

1 **Repeat UAV photogrammetry to assess calving front dynamics at a large**
2 **outlet glacier draining the Greenland Ice Sheet**

3 J. C. Ryan¹, A. L. Hubbard¹, J. Todd², J. R. Carr¹, J. E. Box³, P. Christoffersen², T. O. Holt¹
4 and N. Snooke⁴

5 ¹Centre for Glaciology, Institute of Geography and Earth Sciences, Aberystwyth University,
6 Aberystwyth, SY23 3DB, UK

7 ²Scott Polar Research Institute, University of Cambridge, Cambridge, UK

8 ³Geological Survey of Denmark and Greenland, Copenhagen, Denmark

9 ⁴Department of Computer Science, Aberystwyth University, Aberystwyth, SY23 3DB, UK

10
11 *Correspondence to:* Jonathan Ryan (jor44@aber.ac.uk)

12 *Technical correspondence to:* Neal Snooke (nns@aber.ac.uk)

13
14 **Abstract**

15 This study presents the application of a cost-effective (< US\$2,000), unmanned aerial vehicle
16 (UAV) to investigate frontal dynamics at a major marine-terminating outlet glacier draining
17 the western sector of the Greenland Ice Sheet. The UAV was flown over Store Glacier on
18 three sorties during summer 2013 and acquired over 2,000 overlapping, geo-tagged images of
19 the calving front at a ~ 40 cm ground sampling distance. Stereo-photogrammetry applied to
20 these images enabled the extraction of high-resolution digital elevation models with an
21 accuracy of ± 1.9 m which were used to quantify glaciological processes from early July to
22 late August 2013. The central zone of the calving front advanced by ~ 500 m whilst the
23 lateral margins remained stable. The orientation of crevasses and surface velocity field
24 derived from feature tracking indicate that lateral drag is the primary resistive force and that
25 ice-flow varies across the front, from 2.5 m d^{-1} at the margins to in excess of 16 m d^{-1} at the
26 centreline. Ice flux through the calving front is $3 \times 10^7 \text{ m}^3 \text{ d}^{-1}$, equivalent to 11 Gt a^{-1} ,

27 comparable to recent flux-gate estimates of Store Glacier's annual discharge. Water-filled
28 crevasses were observed throughout the observation period, but covered a limited area (0.025
29 - 0.24% of the surveyed area) and did not appear to exert any significant control over calving.
30 We conclude that the use of repeat UAV surveys coupled with the processing techniques
31 outlined in this paper have a number of important potential applications to tidewater outlet
32 glaciers.

33 **1. Introduction**

34 Observational and modelling studies have demonstrated that Greenland's marine outlet
35 glaciers have a complex and potentially non-linear response to both environmental forcing
36 (e.g. Vieli et al., 2001; Benn et al., 2007; Holland et al., 2007; Howat et al., 2010; Hubbard,
37 2011; Joughin et al., 2012; Walter et al., 2012; Carr et al., 2013) and to changes in front
38 position (Howat et al., 2007, Luckman et al., 2006, Joughin, 2008). To quantify these
39 processes and feedbacks, regular and accurate high-resolution measurements are required to
40 capture the key spatio-temporal linkages between rates of ice calving, flow, surface lowering
41 and frontal advance/retreat. Despite significant advances in satellite remote-sensing,
42 limitations of spatial resolution (e.g. MODIS) and/or frequency of repeat imagery (e.g.
43 Landsat or TerraSar-X (TSX)) renders detailed, day-to-day analysis of calving front
44 dynamics unfeasible. On the other hand, acquisition of digital imagery from UAVs combined
45 with the development of stereo-photogrammetry software has enabled the provision of high-
46 resolution, 3D geo-referenced data on demand for geo-science applications (e.g. d'Oleire-
47 Oltmanns et al., 2012; Hugenholtz et al., 2012, 2013; Whitehead et al., 2013; Lucieer et al.,
48 2014). This represents an effective, cost effective technique for acquiring aerial data in
49 remote, hazardous and/or inaccessible regions and recent applications for emerging snow and
50 ice investigation abound the web (for example, see the highly informative site of Matt Nolan
51 (<http://www.drmattnolan.org/photography/2013/>)). To date, published (peer-reviewed)

52 application appears to be limited to the investigation of inter-annual changes of a land-
53 terminating glacier on Bylot Island, Canadian Arctic (Whitehead et al., 2013).

54 Between July and August 2013, an off-the-shelf, fixed wing UAV equipped with a compact
55 digital camera flew three sorties over the calving front of Store Glacier, West Greenland. The
56 aerial photographs obtained during these flights were used to produce high-resolution (~ 40
57 cm (Table 1)) digital elevation models (DEMs) and orthophotos of the glacier terminus.
58 These data allowed the investigation of the spatially complex and time-varying glaciological
59 processes operating at the glacier's calving front. The aim of this paper is to:

- 60 1) Detail the UAV, in terms of its payload and camera settings, and its specific
61 deployment to Store Glacier.
- 62 2) Describe the techniques used for processing the aerial images and quantifying
63 glaciological processes.
- 64 3) Discuss the significance of the data we obtained which includes calving events, the
65 character, orientation and morphology of crevasses, surface velocities, ice discharge
66 and changes in thickness and position of the calving front.

67 **2. Data and methods**

68 **2.1. Study site**

69 Store Glacier is a large marine-terminating (tidewater) outlet glacier located in the
70 Uummannaq District of West Greenland (Fig. 1). The calving front has a width of 5.3 km and
71 an aerial calving front (freeboard) of up to 110 m a.s.l. (Ahn and Box, 2010). Aerial
72 photography from 1948 reveals that Store Glacier's frontal position has remained stable over
73 the last 65 years (Weidick, 1995). Seasonally, the calving front exhibits advance and retreat
74 of up to 400 m (Howat et al., 2010). These fluctuations appear to coincide with the winter
75 formation and spring break out of the sea-ice mélange, a rigid conglomeration of calved ice

76 and sea ice. The break down and loss of rigidity of the ice mélange with increased air
77 temperature from May to June coincides with a synchronous 14 and 30% increase in velocity
78 near the calving front suggesting that the mélange directly buttresses flow in winter and
79 spring (Ahn and Box, 2010; Walter et al., 2012). After the ice mélange breaks out
80 completely, Walter et al. (2012) observed diurnal changes in surface velocity that appear to
81 correspond to tidal fluctuations. This study focuses specifically on glacier dynamics during
82 the melt season under open-water, tidal modulation of ice flow.

83 **2.2.UAV platform**

84 The UAV airframe is an off-the-self ‘Skywalker X8’ (www.hobbyking.com) which has a
85 wing-span of 2.12 m and is made from expanded polypropylene (EPP) foam (Fig. 2). For this
86 deployment, the X8 was powered by two 5Ah 4-cell (14.8 V) Lithium Polymer batteries
87 driving a 910 W brushless electric motor turning an 11 x 7 foldable propeller. In this
88 configuration, the X8 has a flying mass of ~ 3 kg (including 0.7 kg payload), which allows a
89 cruising speed of around 55 - 70 km per hour with a maximum range of ~ 60 km in relatively
90 calm conditions at constant altitude. A small propeller/high-revolution motor combination
91 was chosen to provide maximum instantaneous thrust to ensure a clean launch (for novice
92 operators) and to handle the potentially strong katabatic winds encountered during its 40 km
93 sortie.

94 The autopilot is an open-source project called ‘Ardupilot’ (<http://ardupilot.com/>) based on a
95 Atmel 2560 8bit microcontroller and standard radio control parts including 2.4 GHz radio
96 control and pulse-width modulation (PWM) controlled servos for aileron and elevon control
97 (Fig. 2). Ardupilot implements a dual-level proportional-integral-derivative (PID) controller
98 architecture. The lower level controls flight stabilisation and the higher level controls based
99 navigation. Tuning of the PID parameters is necessary to suit the mass and dynamics of the

100 airframe to ensure accurate stabilisation without pitch/roll oscillation (lower-level controller)
101 or flight path weaving (higher-level controller). The autopilot allows the UAV to fly
102 autonomously according to a pre-programmed flight path defined by a series of waypoints
103 chosen by the user. The autopilot utilises a GPS for navigation, a triple axis accelerometer
104 and gyro for stabilisation, and a barometric pressure sensor for altitude control and these
105 parameters are logged to memory at 10 Hz throughout the flight (Fig. 2).

106 The advantage of this package is that it can be assembled within a day from off-the-shelf
107 parts and is cost-effective at less than US\$2,000. The X8 is also relatively straightforward to
108 fly, robust, easily repairable and floats; all added bonuses when being deployed in remote
109 areas by relative novices. Furthermore, the Ardupilot firmware is open source and hence can
110 be programmed for specific requirements, for example camera triggering (see below).

111 Two lightweight digital cameras were tested at the field site: a Panasonic Lumix DMC-LX5
112 10.1 megapixel (MP) camera with a 24 mm wide-angle zoom lens and a 16.1 MP Sony NEX-
113 5N with a 16 mm fixed focal length lens though results presented here are limited to the
114 former. A SPOT GPS tracking device was also included in the payload to facilitate recovery
115 should a mission fail (which it did). The focal length of the Lumix lens was adjusted to 5.1
116 mm (35 mm equivalent) to allow the widest possible coverage which gave the camera a 73.7°
117 horizontal and 53.1° vertical field of view. A short exposure time of 1/1600 and a focal ratio
118 of 8 were chosen to prevent overexposure and blurring of the ice surface. The Ardupilot
119 open-source code was amended to trigger the camera automatically at user defined time or
120 distance intervals at or between certain waypoints. The cameras were mounted pointing
121 downwards within the X8 airframe using neoprene and velcro straps to dampen vibration in a
122 custom recessed aperture cut in the bottom with a UV filter to protect the lens and seal it.

123 **2.3.Flight planning**

124 Flight planning was carried out using the open-source software, APM Mission Planner
125 (<http://plane.ardupilot.com/>) in conjunction with the 30 m Greenland Mapping Project
126 (GIMP) DEM (Howat et al., 2014). To optimise spatial coverage against required resolution,
127 flight endurance and stability, the UAV was programmed to fly at a constant altitude of 500
128 m a.s.l. (Fig. 1). Based on the camera's focal length and field of view (53.1° by 73.7°) the
129 ground (sea level) footprint at 500 m a.s.l. for each photo was ~450 x 750 m. To ensure
130 coverage of the entire glacier terminus and overlap for successful photogrammetric
131 processing, the four transects broadly parallel to the calving front were flown with ~250 m
132 separation yielding a side overlap between photos of 70% (Fig. 1). The mean ground speed of
133 the UAV was ~70 km h⁻¹ and camera trigger interval was adjusted between surveys. On
134 flights 1 and 2, the interval between camera triggers was 1.5 s corresponding to a forward
135 overlap of 94% and over 1000 geotagged images acquired. Flight 3 had a 2.4 s interval
136 yielding a 90% forward overlap and 581 images (Table 1).

137 UAV operations were based out of a field camp with the advantage of a 50 m area of flat
138 alluvial terrace with relatively boulder/bedrock free ground for manual remote control take
139 off and landing. This location did, however, require a ~10 km transit to the calving front over
140 a 450 m high peninsula which significantly reduced the useful endurance over the target. Of
141 the six sorties flown over outlet glaciers in the region during July and August, 2013, the three
142 over Store Glacier were most successful. Each sortie was 40 km long and ~35 minutes
143 duration after the UAV had attained its operating altitude at the start of the mission and was
144 passed from manual remote-control mode into autopilot mode (Fig. 1). Visual and remote-
145 control contact is lost within a few km of the UAV being placed in autopilot mode hence it is
146 worth having the 3D waypoints and mission plan independently checked.

147 **2.4. Three-dimensional model generation**

148 Three-dimensional data were extracted from the aerial photos using Agisoft Photoscan Pro
149 software (<http://www.agisoft.ru/products/photoscan>). This software's strength lies in its
150 ability to fully automate workflow and enables non-specialists to process aerial images and
151 produce 3D models which can be exported as georeferenced orthophotos and DEMs (e.g. Fig.
152 3, 6). The first stage of processing is image alignment using the structure-from-motion (SFM)
153 technique. SFM allows the reconstruction of 3D geometry and camera position from a
154 sequence of two-dimensional images captured from multiple viewpoints (Ullman, 1979).
155 Photoscan implements SFM algorithms to monitor the movement of features through a
156 sequence of multiple images and is used to estimate the location of high contrast features
157 (e.g. edges), obtain the relative location of the acquisition positions and produce a sparse 3D
158 point cloud of those features. The Ardupilot flight logs of the onboard navigation sensors
159 allow the camera positions and the 3D point cloud to be georeferenced within instrument
160 precision. SFM also enables the camera calibration parameters (e.g. focal length and
161 distortion coefficients) to be automatically refined hence there is no need to pre-calibrate the
162 cameras and lens optics (Verhoeven, 2011).

163 Once the photos have been aligned, a multiview reconstruction algorithm is applied to
164 produce a 3D polygon mesh which operates on pixel values rather than features and enables
165 the fine details of the 3D geometry to be constructed (Verhoeven, 2011). The user determines
166 the precision of the final 3D model based on image resolution and pixel footprint. A medium
167 quality setting was chosen yielding DEMs with between 38 – 40 cm/pixel ground sampling
168 resolution (GSD), which were resampled to a Cartesian 50 cm grid to enable intercomparison
169 (Table 1). Higher resolutions (<30 cm GSD) are attainable but the increase in computational
170 time and the accuracy of georeferencing limits the benefits of such apparent precision.

171 Two problems of accuracy were encountered in DEM production. The first was that
172 Photoscan failed to reconstruct a flat sea level of constant elevation. The second was that the
173 relative positional errors between the DEMs constructed from different sorties were up to 15
174 m. Positional errors were due to: 1) the specified limits of the onboard L1 GPS of ± 5.0
175 metres horizontally and, when combined with the barometric sensor, to a similar accuracy
176 vertically, and 2) the time lag between the camera triggering and actually taking a picture.
177 The time lag was not corrected for in this study and is likely to introduce a few metres of
178 systematic horizontal error for every image. Hence, a secondary stage of processing was
179 carried out which involved 3D co-registration of the DEMs. To do this, the horizontal and
180 vertical coordinates of common control points (CPs) based on distinct features like cliff
181 bases, large boulders and promontories were extracted from the georeferenced orthoimages.
182 The CPs that were at sea level were nominally given elevation values of zero, re-imported
183 into Photoscan and subsequently reprocessed along with a geodetic GPS ground CP located
184 at 70.401°N, -50.6654°E and 335.85 m altitude on the bedrock headland overlooking the
185 glacier's northern flank. During this secondary stage of processing, Photoscan's optimization
186 procedure was run to correct for possible distortions. After processing the relative horizontal
187 errors between the three DEMs was reduced to < 1 m and gave a flat sea level across the
188 glacier front with a vertical error at the known (GPS) CP of 1.4 m. The georeferenced 3D
189 DEMs and orthophotos were then exported at 50 cm pixel size for further analysis in ArcGIS
190 and ENVI software packages.

191 **2.5. Analysis**

192 Changes in calving front positions were obtained from these data combined with a Landsat 8
193 panchromatic image obtained on 12 June (Fig. 3B). Each calving front position was digitized
194 according to the procedure outlined by Moon and Joughin (2008) whereby a polygon of the

195 calving front retreat or advance is digitized and divided by the width of the glacier. This
196 method has been used in previous studies (e.g. Howat et al., 2010; Schild and Hamilton,
197 2013) and enables intercomparison of results. Surface elevation change was calculated from
198 the residual difference of the DEMs (Fig. 3A).

199 Ice flow across the terminus region was calculated by feature tracking performed on
200 successive orthophotos using the ENVI Cosi-CORR software module (Fig. 4B). These
201 velocities were then used to estimate ice flux through the calving front for the same period
202 under the assumption of plug flow (uniform velocity profile with depth) and using an calving
203 front cross-section obtained from single-beam echo sounder bathymetry across the calving
204 front obtained by boat in 2010 and 2012. The frontal cross-section was divided into 10 m
205 vertical strips and each one assigned a horizontal velocity value (Fig. 4A). The floatation
206 depth and buoyancy ratio across the calving front was calculated using the ice surface
207 (freeboard) elevation and total ice thickness with a value for the density of ice of 917 kg m^{-3}
208 for sea water of 1028 kg m^{-3} (Fig. 5A) following Motyka et al. (2011).

209 To investigate the distribution and patterns of crevassing, each DEM was Gaussian filtered at
210 200 pixels (100 m) in ArcGIS and subtracted from the original DEM to yield the pattern of
211 negative surface anomalies. These anomalies were converted into polygons to map and hence
212 quantify crevasse distribution and character (Fig. 6A). The resulting polygons were enclosed
213 by a minimum bounding rectangle, which allowed the orientation, width, length and depth of
214 crevasses to be extracted (Fig. 6A, Table 2). Water-filled crevasses were automatically
215 located in the ENVI package using the supervised maximum likelihood classification (MLC)
216 method. Representative training samples for water-filled areas were chosen from the colour
217 composite orthophoto (Fig. 6B). The trained tool then classifies pixels that are interpreted as
218 water into the desired class. The resulting raster image was converted into a shapefile and

219 used to mask and define the area of the water-filled crevasses across the terminus. These
220 procedures allow thousands of crevasses in multiple orthoimages and DEMs to be quantified
221 easily without the difficulties and dangers associated with direct field measurements.

222 **2.6.Uncertainties and limitations**

223 The relative horizontal uncertainties between the DEMs were investigated by feature tracking
224 the stationary bedrock at the sides of the glacier. The RMS horizontal displacement was ± 1.0
225 m which provides us with an approximate error estimate. The relative vertical uncertainties
226 between the DEMs were estimated by calculating elevation differences between bedrock
227 areas, which reveal an error estimate was ± 1.9 m. The two-stage procedure outlined in
228 Section 2.4 therefore enabled us to improve the relative positional uncertainties from nearly
229 15 m to about 1 m. For future studies, it is thought that several CPs on the bedrock either side
230 of the glacier front would further reduce these uncertainties. A telemetric differential GPS
231 deployed on or near the calving front, which is sufficiently large/bright to identify within the
232 aerial imagery would allow further ground control in the centre of DEMs, away from bedrock
233 CPs.

234 Due to the lack of reflected light from deep crevasse recesses, the DEM generation process
235 cannot quantify the narrowest sections of all fractures and resultant crevasse depths are
236 therefore a minimum estimate. The technique is also clearly limited to line of sight
237 precluding narrow fractures which extend for tens of centimetres horizontally and potentially
238 up to a few metres vertically (Hambrey and Lawson, 2000; Mottram and Benn, 2009).

239 Finally, there are a number of practical difficulties when operating an autonomous aircraft
240 over such ranges in remote and inaccessible environments. Mission planning is critical;
241 knowledge of the local weather conditions, as well as up-to-date satellite imagery and DEMs
242 are a prerequisite for a successful outcome.

243 3. Results

244 Three successful UAV sorties were flown over Store Glacier calving front providing
245 imagery, orthophotos and DEMs on 1 and 2 July and the 23 August, herein referred to flights
246 and associated products 1 to 3, respectively (Table 1). The interval between flights 1 and 2
247 was 19 hours and comparison between these outputs enables identification of processes
248 operating over a daily (short) timescale, be it a very specific snapshot. The third sortie was
249 flown 52 days later and comparison between these outputs enables investigation of late-
250 seasonal change. The four transects flown captured just over 1 km of Store Glacier from its
251 calving front and herein, ‘the terminus’ refers to this section of the glacier.

252 3.1.Short timescale calving and surface elevation change

253 Residual elevation change between 1 and 2 July (Fig. 3A) reveals that the front retreated in
254 two sections by up to 50 and 80 m respectively. Calving event A resulted in a 450 m wide
255 section of the terminus retreating by between 20 and 50 m, whilst event B produced between
256 20 m and 80 m of retreat across a 400 m section (Fig. 3A). In addition to these two calving
257 events (which are discussed in section 3.6), the central 4.5 km frontal section advanced
258 between 12 m to 16 m (Fig. 3A). At its lateral margins, the calving front shows no discernible
259 systematic change though there are isolated, small calving events, for example, within 50 m
260 of the southern flank (Fig. 3A). Upstream of the calving front, there is no net change in mean
261 surface elevation away from the front and the dappled pattern of residual elevation change is
262 a result of the advection of crevasses and seracs. Successive long profiles of the terminus
263 between the 1 and 2 July reveal specific down-glacier crevasse advection with flow (Fig. 6) at
264 a rate of 5 and 16 m d⁻¹ on Profile 1 and 2, respectively. These results provide estimations of
265 surface velocities which are confirmed by feature tracking in the Section 3.4.

266 3.2.Seasonal timescale calving front position and surface elevation change

267 Over the entire melt season, larger fluctuations in calving front position are observed (Fig.
268 3B). Over the 19 day period from 12 June to 1 July, mean frontal retreat was 160 m (Fig. 3C)
269 and between 2 July and 23 August, the calving front advanced by an average of ~110 m to a
270 position similar to that in 12 June (Fig. 3D). These mean values, however, do not convey the
271 full extent and detail of the changes observed in the calving front. For example, the central
272 section of the calving front retreated by up to 525 m between the 12 June and 1 July and
273 advanced by up to 450 m between 2 July and 23 August (Fig. 3B). Furthermore, the lateral
274 margins of Store Glacier (the southern 850 m and the northern 1.5 km) are relatively stable
275 with < 50 m change in position. Over the 52 day period between 2 July (Flight 2) and 23
276 August (Flight 3) widespread surface lowering of 6.1 m (or 0.12 m d⁻¹) was observed across
277 Store Glacier terminus (Fig. 4A), which is significantly larger than the estimated vertical
278 uncertainties of the DEMs (± 1.9 m). Despite the same dappled patterns caused by local
279 advection of crevasses and seracs, there is significant lowering 1km upstream of the calving
280 front, which we discuss in Section 4.2.

281 **3.3. Bathymetry**

282 The deepest sector of the calving front is located 1 km south of the centreline and exceeds
283 540 m below sea level (Fig. 5A). This 200 m wide sector also corresponds to the greatest
284 thickness of ~ 600m. To the south of this deepest point, the bottom rises rapidly to a 200 m
285 deep shelf located 500 m from the flank. To the north of the deepest point, the bottom
286 shallows more gently to within 400 m where it becomes steeper towards the fjord wall.

287 **3.4. Surface velocities**

288 Maximum surface flow velocities of 16 m d⁻¹ between 1 and 2 July are consistent with results
289 obtained in previous studies using other techniques, such as feature tracking images from a
290 land-based time-lapse camera (between 11 and 15 m d⁻¹) (Ahn and Box, 2010; Walter et al.,

291 2012). The spatial pattern of surface flow from feature tracking of images between the 1 and
292 2 July varies considerably across the terminus of Store Glacier (Fig. 4B) attaining velocities
293 of 16 m d^{-1} (5.8 km a^{-1}) near the centre of the glacier down to 2.5 m d^{-1} at the lateral flanks.
294 Surface velocities are related to slope, depth, thickness and distance from the lateral margins
295 (Fig. 5C, D). As would be expected, maximum velocities ($> 14 \text{ m d}^{-1}$) correlate roughly with
296 maximum depth and towards the north flank are linearly correlated ($R^2 = 0.90$) with frontal
297 depth (Fig. 5C). Towards the southern flank the relationship is less apparent especially
298 between 200 to 350 m depths. There is a strong correlation between velocities and distance
299 from the lateral margins which can be approximated by a power function ($R^2 = 0.90$) (Fig.
300 5D). Although application of the floatation criteria indicates that parts of calving front are
301 buoyant (Fig. 5A), side-scan sonar observations reveal that the glacier front was resting on
302 the bottom in 2010 and 2012. When the surface flow pattern is combined with frontal
303 bathymetric data we estimated that the mass flux through the calving front of Store Glacier
304 was $3 \times 10^7 \text{ m}^3 \text{ d}^{-1}$, equivalent to $\sim 11 \text{ Gt a}^{-1}$.

305 Seasonal flow patterns were not obtainable between 2 July and 23 August as the majority of
306 any matching features within the study area required for tracking had already calved into the
307 ocean. Furthermore, it is likely that the morphology of many crevasses and seracs will have
308 changed significantly through melt and deformation and would not be recognised by the
309 cross-correlation procedure.

310 **3.5.Crevassing**

311 The morphology and orientation of crevasses varies markedly across the terminus (Fig. 6).
312 The largest crevasses occur in a sector south of the glacier centre line in zone 4 (Fig. 6, Table
313 2). Here, crevasses have mean minimum depths of 18 m, lengths of 68 m and widths of 31 m.
314 The largest crevasses are up to 30 m deep, over 500 m long and nearly 200 m wide but no

315 crevasses that penetrated below sea level were identified. Most crevasses in this region are
316 arcuate with limbs pointing towards the calving front and are orientated obliquely to the
317 direction of ice flow (Fig. 6). This arcuate morphology of crevasses continues across the
318 central 3 km of the terminus in zone 3 (Fig. 6). Here, crevasses have mean a depth of 10.5 m,
319 length of 50 m and widths of 18 m (Table 2). In zone 2, 300 to 500 m from the northern flank
320 crevasses are aligned obliquely to the direction of ice flow (30 - 45°). Up to the fjord walls in
321 zones 1 and 5, crevasses are generally orientated parallel to the ice flow ($> 15^\circ$) (Fig. 6, Table
322 2) and are much smaller with a mean lengths of 22 m and width of 8 m (Table 2). No
323 discernible difference in average crevasse depths, lengths or widths was observed between
324 the early July and late August and the pattern and character of crevassing was very similar.

325 Water-filled crevasses were clustered in zone 4, coinciding with the sector of larger crevasses
326 (Fig. 6B). Water-filled crevasses covered 12,000 m² or 0.24 % of the survey area (to ~ 1 km
327 from the calving front) (Table 1) on 2 July. Some 42 individual water-filled crevasses were
328 identified with the largest having an area of 1,200 m². By 23 August, the number, size and
329 total area of water filled crevasses were lower: only 10 water-filled crevasses could be
330 identified, the largest of which was 400 m² and with a total area of 1,230 m² (0.025% of the
331 survey area). We were not able to ascertain the depth of water in the crevasses as no
332 crevasses could be identified which drained or filled between observations but this would be
333 a specific aim of future studies which, with regular sorties, could potentially measure the
334 depth of a crevasse before filling or after drainage or otherwise exploit light reflectance
335 relationship with water depth.

336 Successive profiles of the terminus from 1 and 2 July demonstrate how the UAV surveys are
337 capable of capturing the displacement of crevasses, which advect downstream at a rate of 5
338 and 16 m d⁻¹ in Profiles 1 and 2, respectively (Fig. 6). The techniques used in this study are

339 therefore capable of identifying changes in crevasses geometry, particularly width and depth
340 through time.

341 **3.6. Calving events**

342 The two calving events identified between 1 and 2 July appear to take place under contrasting
343 conditions. Event A consisted of the calving of multiple, relatively small ice blocks with the
344 glacier failing along two main crevasses located 30 and 50 m behind the calving front. These
345 crevasses were between 8 and 10 m deep, respectively and in this instance, the crevasses
346 located closest to the front were the ones that failed. Event B appears to be a single large
347 event caused by the fracturing of a series of parallel crevasses which were up to 14 m deep
348 and 60 m behind the calving front. Unlike, calving event A, the crevasses that failed in event
349 B were not the closest to the calving front. Indeed, there were other crevasses that were
350 deeper and located nearer to the front, yet did not calve. Water was not observed in any of the
351 crevasses along which calving took place.

352 **4. Discussion**

353 **4.1.Changes occurring over a daily timescale**

354 The orientation of crevasses suggests that lateral drag is an important resistive stress on Store
355 Glacier. The lateral margins of the Store are characterised by crevasses that are orientated
356 parallel to the direction of flow which suggests that they have formed in response to simple
357 shear stresses associated with the drag of the fjord walls (Fig. 6) (Benn and Evans, 2010).
358 The importance of lateral drag is further demonstrated by the morphology of crevasses found
359 near the glacier flowline (Fig. 6). Their arcuate nature indicates that the principal tensile
360 stresses operating on the ice have been rotated by lateral gradients in ice velocity. These
361 gradients are caused by the simple shear stress between the fjord walls and the margins of the
362 glacier which cause the ice to flow slower (Fig. 4B) (Benn and Evans, 2010).

363 The simple shearing caused by velocity gradients is further demonstrated by the differing
364 relationship between velocity and depths between the north and south side of the glacier (Fig.
365 5C, D). On the north side, the velocity increases gradually from the fjord wall to the centre of
366 the glacier, reflecting the gradual deepening of bathymetry and the resulting decrease of basal
367 and lateral drag. On the south side, the velocities are higher than the north side for given
368 depths and distances from the lateral margins (Fig. 5C, D). We hypothesize that, because the
369 deepest part of the glacier is situated 1 km south of the centreline, the ice on south side is
370 more influenced by faster flowing ice which exerts a simple shear stress on the shallower,
371 adjacent ice (250 – 400 m thick). This causes the shallow ice to flow faster than ice with
372 similar thicknesses and distance from the lateral margins on the north side (Fig. 5C).

373 The mass flux through the calving front was calculated at $3 \times 10^7 \text{ m}^3 \text{ d}^{-1}$ which needs to be
374 balanced by three main frontal processes: calving, submarine melting and advective advance.
375 Both calving and advance were observed in this study but it is likely that submarine melting
376 also has a large role in ice output at a daily timescale. For example, Xu et al. (2013) used
377 oceanographic data to calculate a melt water flux of between 0.5 and $1.1 \times 10^7 \text{ m}^3 \text{ d}^{-1}$ from
378 Store Glacier in August, 2010 equivalent to 17 - 37% of the mass flux calculated in by our
379 study. For comparison, Rink glacier has an ice flux of $3.0 \times 10^7 \text{ m}^3 \text{ d}^{-1}$ of which 27% is
380 estimated to be lost through submarine melting each day (Enderlin and Howat, 2013).

381 **4.2. Changes occurring over a seasonal timescale**

382 The lack of variation in the position of the lateral margins of the glacier shows that a balance
383 is maintained between the ice flux input and submarine melting and calving output in this
384 zone throughout the melt season. The balance could be explained by the mechanism of
385 calving events. At the lateral margins calving is characterised by small, regular events such as
386 calving event A (Fig. 3A). The regularity of these small events means that any small advance

387 or retreat is regulated almost instantly by changes in calving rate which returns the lateral
388 margins of the glacier to the same position. Calving rate could also be moderated by changes
389 in the bathymetry. When the lateral margins advance, calving rates increase due to the abrupt
390 deepening of the bathymetry seaward of the lateral margins of the glacier which cause basal
391 drag to be reduced. Ice flow acceleration can lead to increased longitudinal stretching and
392 deeper crevassing, thereby increasing calving rate and leading to retreat to its original,
393 bathymetrically-pinned position.

394 The centre of the calving front is much more active with calving and submarine melt rates
395 that vary on a seasonal timescale. We propose that the main cause of variability is due to
396 calving rates which are highly irregular throughout the melt season (Jung et al., 2010). Our
397 observations also support the suggestion that calving rates are dominated by major calving
398 events which have a time interval of around 28 days (e.g. Jung et al., 2010). If the calving
399 front advances for 28 days at 16 m d^{-1} , it will advance 448 m. A large, single calving event
400 can then cause a retreat of $\sim 448 \text{ m}$ and which would explain the variation in the position of
401 the calving front during the melt season (Fig. 3B). On 25 August 2013, a tabular iceberg with
402 a length of $\sim 500 \text{ m}$ was observed to calve from the central zone of Store Glacier.

403 Towards the end of the melt season (23 August), widespread surface lowering of 0.12 m d^{-1} is
404 observed (Fig. 4A). A simple degree-day model shows that part of this lowering can be
405 attributed to ablation. Average daily air temperatures were recorded 4 m a.s.l. at a weather
406 station located near the UAV launch site (Fig. 1) and, using a factor of 6 – 10 mm per degree
407 per day (Hock et al. 2005), surface lowering due to ablation is estimated at $0.038 - 0.064 \text{ m d}^{-1}$
408 ¹. Therefore surface ablation alone cannot account for all the observed thinning. Other
409 hypotheses for surface lowering include a dynamic response to flow acceleration. However,
410 Ahlstrom et al. (2013) note that between July and August, surface velocities $> 8 \text{ km}$ upstream
411 of the calving front usually decrease. This raises interesting questions about the timescale

412 over which dynamic thinning occurs and the relationship between the processes occurring at
413 the terminus and the processes occurring upstream. But it is probably beyond the scope of the
414 data obtained in this study to answer these questions sufficiently.

415 Another important observation is the order of magnitude reduction of the area of water-filled
416 crevasses between early July and late August (Fig. 6). Surface air temperatures are likely to
417 influence the extent of water-filled crevasses. Data from the weather station, reveal that daily
418 air temperatures averaged 6 °C during the four days prior to the UAV sortie on the 2 July. In
419 contrast, average temperatures were 3.5 °C on the four days prior to the UAV sortie on 23
420 August. These data signify a potential mechanism by which increased air temperatures could
421 increase calving rate and cause changes to the ice dynamics (Benn et al., 2007). Water-filled
422 crevasses are hypothesized to penetrate deeper than crevasses without water (Weertman,
423 1973; Van der Veen, 1998; Benn et al., 2007) and hence act as foci for calving. The calving
424 events observed in this study did not involve any water-filled crevasses. It remains to be seen
425 whether water-filled crevasses have an impact on calving from Store Glacier but our limited
426 results do not support this hypothesis.

427 **5. Conclusions and future directions**

428 A UAV equipped with a commercial digital camera enabled us to obtain high resolution
429 DEMs and orthophotos of the calving front of a major tidewater glacier at an affordable price.
430 Airborne LiDAR currently presents the only alternative method for acquiring DEMs with
431 comparable accuracy and precision. However, to fly consecutive sorties in a remote
432 environment would be far more expensive and with sufficient ground control points the
433 digital photogrammetry approach may exceed the accuracy of this technique.

434 The three sorties flown enabled key glaciological parameters to be quantified at sufficient
435 detail to reveal that the terminus of Store Glacier is a complex system with large variations in

436 crevasse patterns surface velocities, calving processes, surface elevations and front positions
437 at a daily and seasonal timescale. Surface velocities vary across the terminus and are
438 influenced by both basal and lateral drag (Fig. 4B, 5C, D). The oblique orientation and
439 arcuate nature of crevasses suggests that the principal extending strain rate is orientated
440 obliquely to the direction of flow and we therefore propose that resistive stresses at the
441 terminus of Store Glacier are dominated by lateral drag (Fig. 6). With this in mind, the retreat
442 of Store into a wider fjord could significantly increase the ice discharge. We estimated that
443 the current ice flux of Store was $3 \times 10^7 \text{ m}^3$ and observed a small terminus advance between 1
444 and 2 July (Fig. 3A, 5A). This advance shows that, during this period, the sum of calving and
445 submarine melt rates are less than the ice flux. Calving is, however, an irregular process and
446 the fact that the position of the calving front returned to its 12 June position by 23 August
447 suggests that over this timescale calving and submarine melt rate balance ice flux (Fig. 3B).
448 Water-filled crevasses covered 0.24% of the survey area on 2 July but this fell to 0.025% on
449 23 August (Fig. 6). It remains to be seen whether water-filled crevasses are more likely to
450 initiate calving events but these data signify a potential mechanism by which increased air
451 temperatures could increase calving rate and impact on ice dynamics.

452 Future studies, with a larger number of sorties could be used to compare and investigate
453 further glaciological changes over a more continuous timespan. There is also the possibility
454 of a more varied payload with radiation, albedo and other fine-band sensors as well as a laser
455 altimeter for constant height above ground surveys. Therefore there are many potential
456 cryospheric applications for investigation of sea ice, outlet glacier and ice masses that can be
457 achieved with the use of repeat UAV surveys. For marine-terminating outlet glaciers, a UAV
458 carrying a digital camera would be sufficient to investigate the following projects:

- 459 • Analysis of the thickness and back-stress exerted by the ice mélange during the winter
460 and the effect of its break up on outlet glacier flow, calving rate and character.

- 461 • Seasonal changes in the depth, density, orientation and nature of crevassing and their
462 impact on calving rate and character.
- 463 • The influence of daily to seasonal melt and supraglacial lake drainage on downstream
464 dynamics and calving.
- 465 • Analysis of daily to seasonal fluctuations in terminus position and impact on upglacier
466 flow.
- 467 • Determination of bulk frontal discharge and associated thinning throughout the
468 season.

469

470

471

472

473

474

475

476

477

478

479

480

481 **Tables**

482 **Table 1.** Attributes of the flight surveys and image acquisition of the UAV

Flight no.	Date	Interval between pictures (s)	No. images	Glacier coverage (km ²)	Resolution of DEM (cm/pixel)
1	01 July	1.55	611	3.17	40
2	02 July	1.51	1051	4.95	38
3	23 August	2.36	567	5.02	39

483

484 **Table 2.** Attributes of mean crevasse width, length and orientation in each zone labelled in

485 Figure 5. Orientations are measured along the long-axis of each crevasse and are in respect to

486 the direction of flow which is 0°.

Zone	Mean width (m)	Mean length (m)	Mean orientation (°)
Zone 1	3.6	9.4	9.2
Zone 2	4.8	14.0	36.7
Zone 3	10.5	32.6	85.1
Zone 4	6.5	17.8	60.4
Zone 5	3.5	8.5	10.8

487

488

489

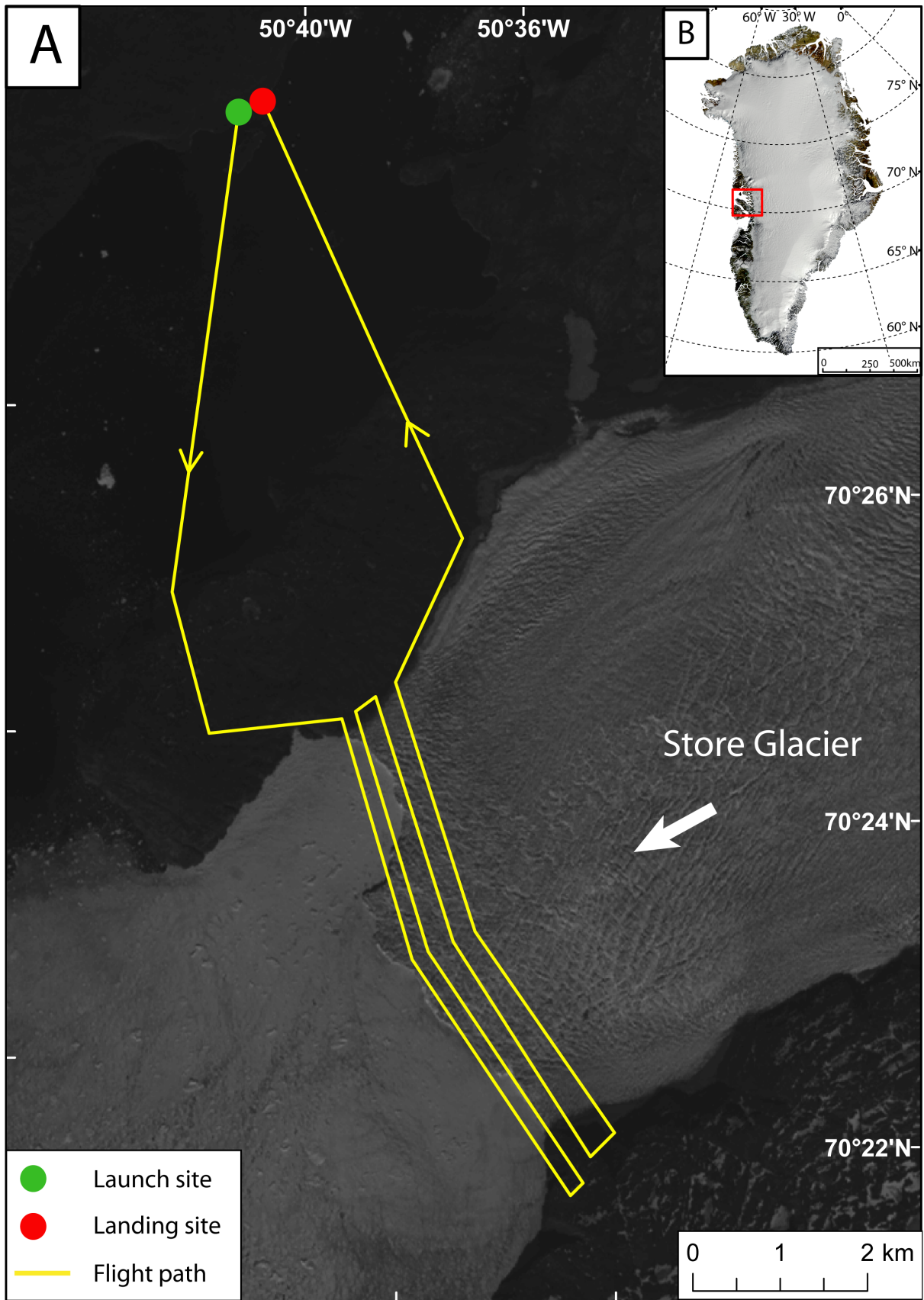
490

491

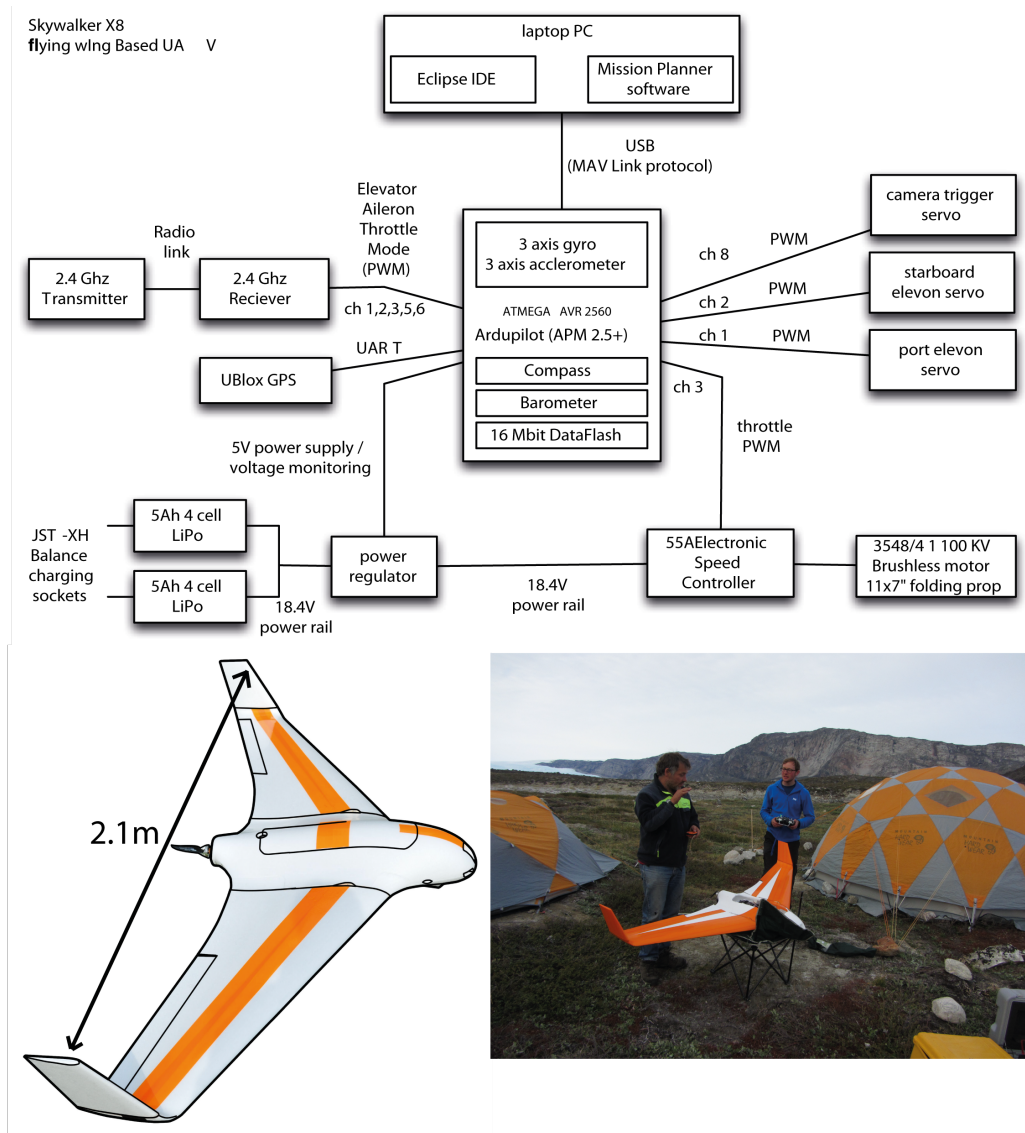
492

493

494

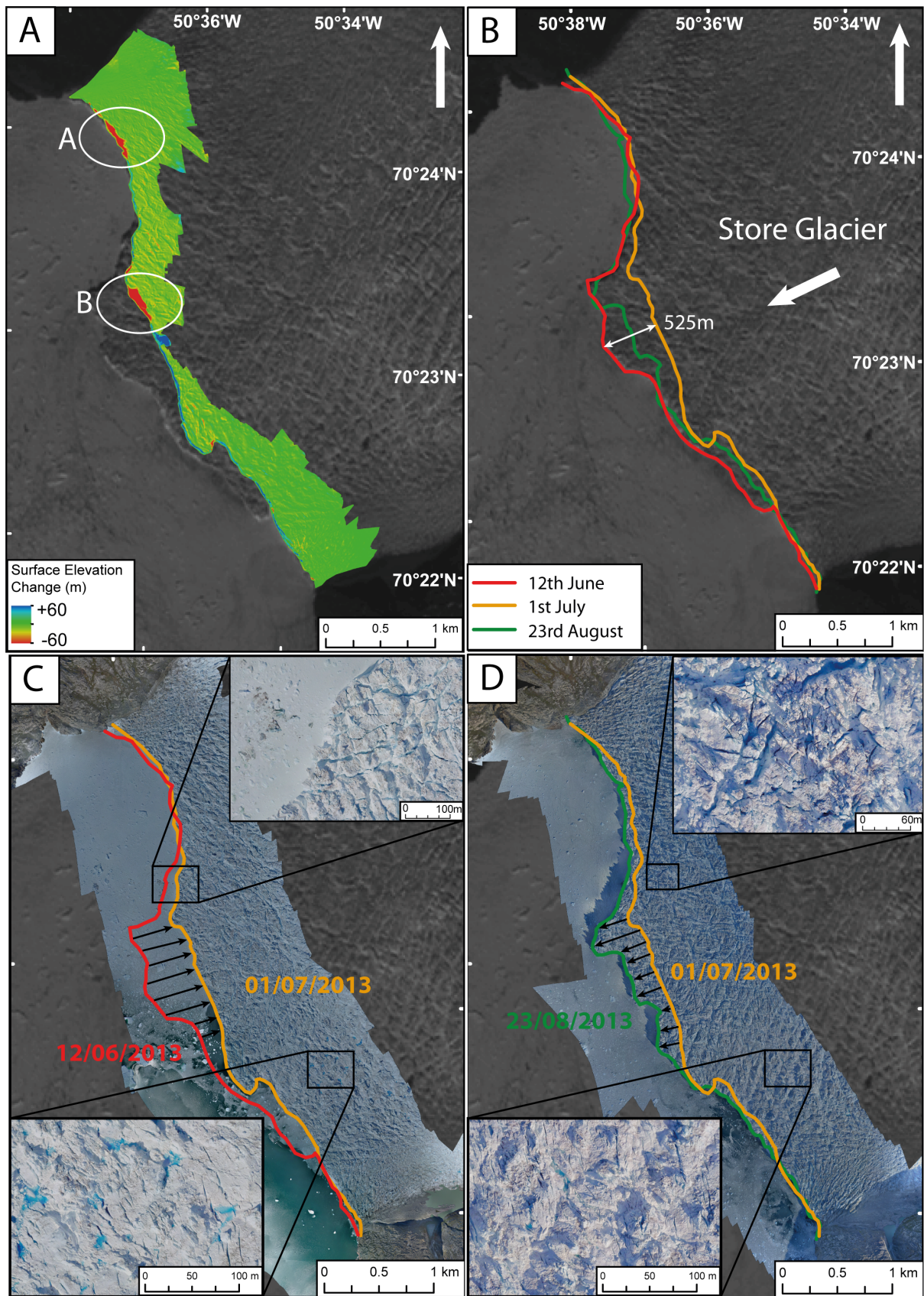


497 **Figure 1.** (A) The planned UAV mission over Store Glacier. The background map is a
 498 Landsat 8 panchromatic image from 12 June 2013. The green and red dots show the
 499 launching and landing sites and the yellow line shows the planned UAV mission. (B)
 500 Location of Store Glacier in the Uummannaq Region, West Greenland on a MODIS mosaic
 501 image of Greenland (Kargel et al., 2012).



502
 503 **Figure 2.** Flowchart of the control set up and picture of the UAV at base camp with the
 504 ‘relative novices’.

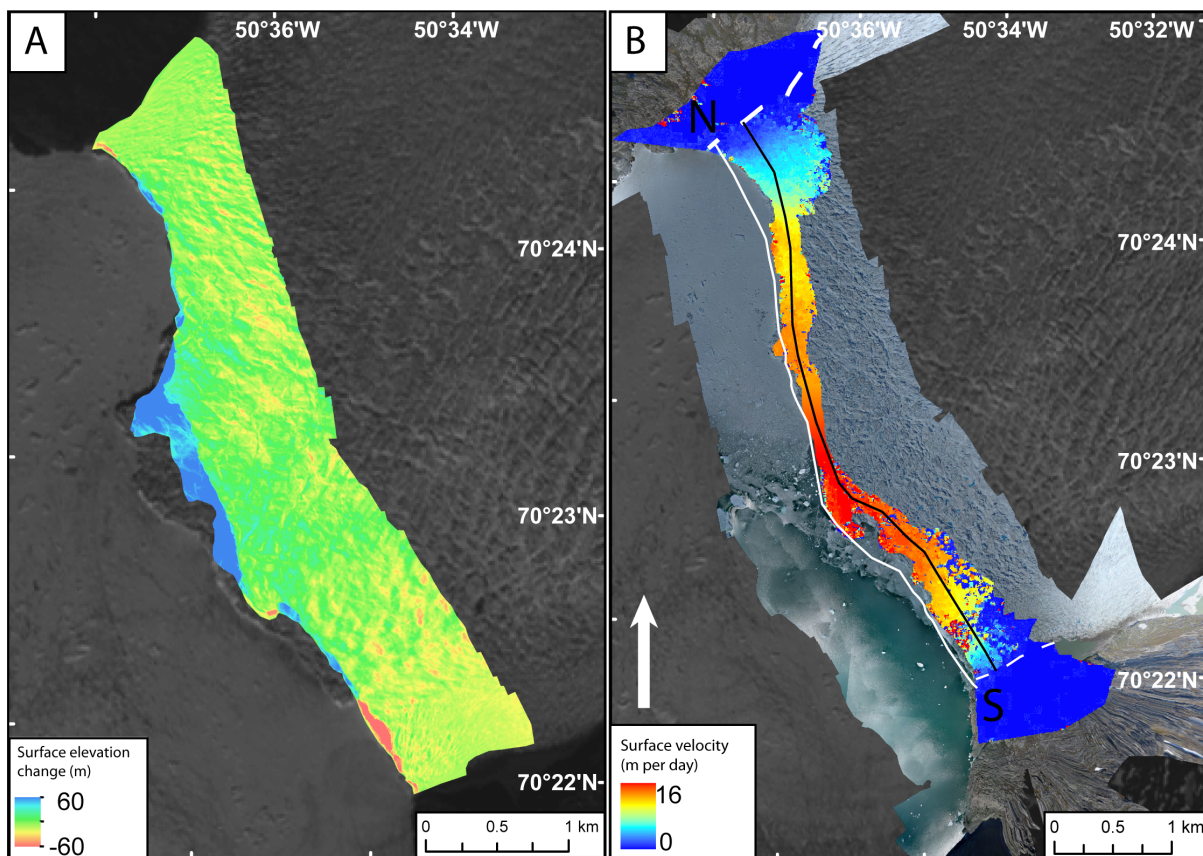
505



506

507 **Figure 3.** (A) Surface elevation difference between two DEMs collected on 1 July and 2 July.
 508 Red areas show elevation loss whilst blue areas show elevation gain. White circles highlight
 509 the calving events that occurred between the two UAV surveys. (B) The position of the
 510 calving front of Store Glacier during the summer of 2013. (C) Calving front retreat observed
 511 between 12 June and 1 July. Inset is an orthorectified image of the water-filled crevasses
 512 observed on 1 July with a pixel resolution of 30 cm. (D) Calving front advance observed
 513 between 1 July and 23 August. Inset is an orthorectified image showing waterfilled crevasses
 514 observed on 23 August. The coverage and size of water-filled crevasses is smaller.

515

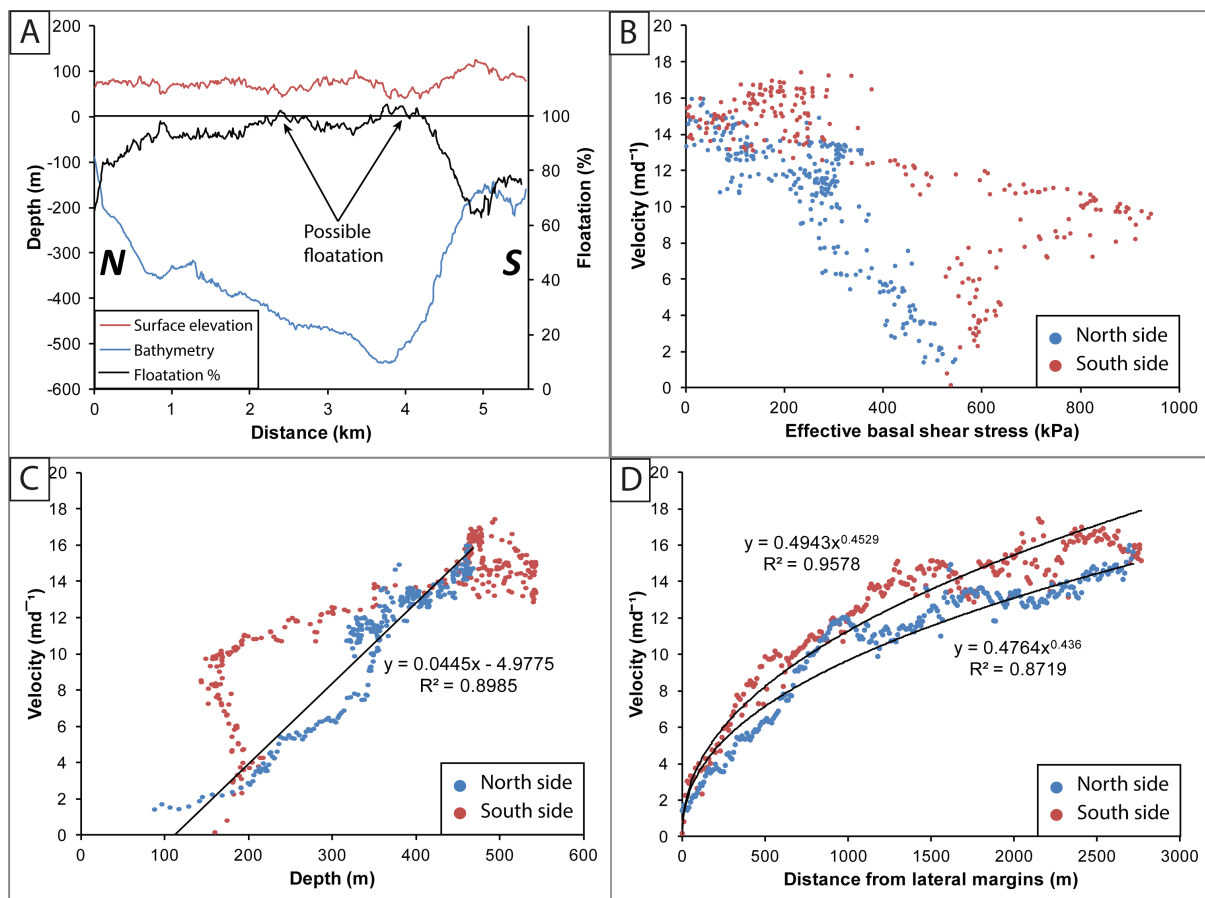


516

517 **Figure 4.** (A) Surface elevation changes between 2 July and 23 August. An average thinning
 518 of 0.12 m d^{-1} was estimated for the surveyed area. (B) The ice flow speed structure of the
 519 terminus of Store Glacier between 1 and 2 July 2013. The centre of the glacier flows at

520 approximately 16 m d^{-1} whilst the margins flow less than 5 m d^{-1} . Dotted white lines show the
 521 lateral margins of the glacier. The black line represents the locations of the horizontal
 522 velocity and surface elevation values that were used to estimate ice flux. The white line
 523 represents the location of the depth values used to estimate ice flux. The cross-section of the
 524 calving front derived from these profiles is displayed in Fig. 4A.

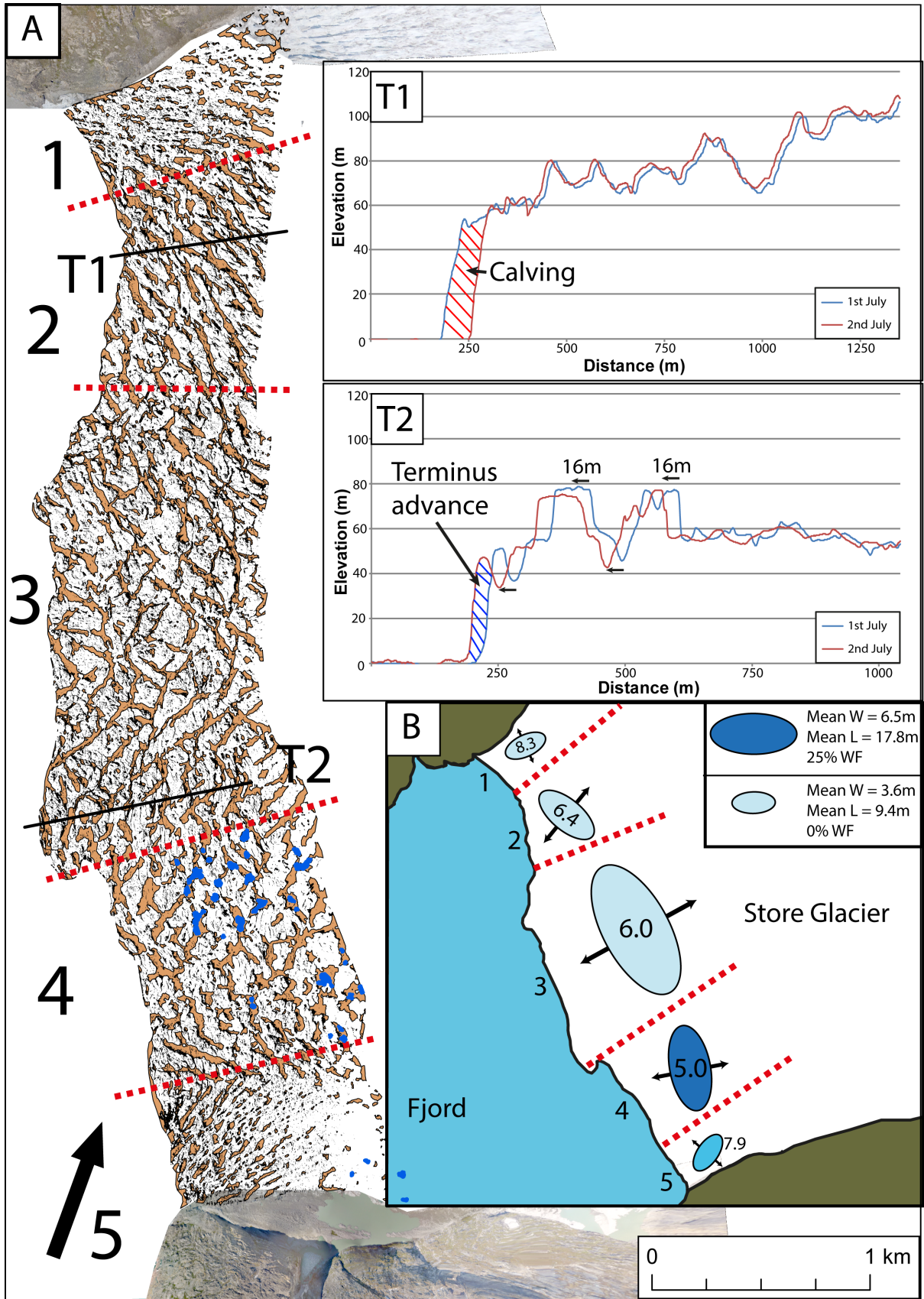
525



526

527 **Figure 5.** (A) Profiles showing the sea floor bathymetry and ice surface elevation at the
 528 calving front. These data were combined with surface velocities to estimate the ice flux of
 529 Store Glacier. Where the floatation percentage is over 100%, it is assumed that the ice is not
 530 thick enough to be fully grounded in hydrostatic equilibrium. (B) The relationship between
 531 effective basal shear stress and velocity. (C) The relationship between depth and velocity. At
 532 depths deeper than 400 m, velocities are fairly constant. The two differing relationships

533 between 150 and 350 m represent velocities from different sides of the glacier. (D)
534 Relationship between velocity and distance from the lateral margins. The positive correlation
535 demonstrates the importance of the resistance provided by the fjord walls although depth also
536 increases with distance from the fjord walls so can also explain this relationship.



538 **Figure 6.** (A) Distribution and patterns of crevasses on Store Glacier. Dry crevasses which
539 are large structural features are shown in orange. Narrower crevasses that are observed in the
540 orthorectified images but whose 3D geometry is not constructed are shown in black. The
541 areas of water-filled crevasses are shown in blue and occur almost exclusively in zone 4. The
542 regions of the terminus that are discussed are designated by the dotted red lines are referred to
543 be the black numbers. Transects 1 and 2 shown in inset demonstrate how crevasses advected
544 downstream between 1 and 2 July. In T1, a series of calving events occurred which are
545 discussed as ‘calving event A’. In T2, the calving front advanced 16 m. (B) Cartoon of the
546 terminus of Store Glacier with ellipsoids proportional to the average length, width and
547 orientation of crevasses shown in (A) for the respective zones. The colour of the ellipsoids
548 represents the proportion of crevasses that are water-filled in each zone where WF refers to
549 water-filled in the legend. The italicized numbers denote the density of crevasses per 10 m² in
550 each zone. Arrows illustrate inferred direction of principal strain.

551 **References**

- 552 Agisoft LLC (2013). Agisoft PhotoScan. <http://www.agisoft.ru/products/photoscan/> (date of
553 access: 14 February 2014).
- 554 Ahlstrøm, A. P., Andersen, S. B., Andersen, M. L., Machguth, H., Nick, F. M., Joughin, I.,
555 Reijmer, C. H., van de Wal, R. S. W., Merryman Boncori, J. P., Box, J. E., Citterio, M., van
556 As, D., Fausto, R. S., and Hubbard, A.: Seasonal velocities of eight major marine-terminating
557 outlet glaciers of the Greenland ice sheet from continuous in situ GPS instruments, *Earth*
558 *Syst. Sci. Data*, 5, 277-287, doi:10.5194/essd-5-277-2013, 2013.
- 559 Ahn, Y. and J. E. Box.: Glacier velocities from time-lapse photos: technique development
560 and first results from the Extreme Ice Survey (EIS) in Greenland, *Journal of Glaciology*, 56,
561 723–734, doi:10.3189/002214310793146313, 2010.

562 Benn, D. I., Warren, C. R., and Mottram, R. H.: Calving processes and the dynamics of
563 calving glaciers, *Earth-Science Reviews*, 82, 143-179, doi:10.1016/j.earscirev.2007.02.002,
564 2007.

565 Benn, D. I., and Evans, D. J. A.: *Glaciers and glaciation*. London: Hodder Education, 2010.

566 Box, J. E., and Decker, D. T.: Greenland marine-terminating glacier area changes: 2000-
567 2010, *Annals of Glaciology*, 52, 91-98, 2011.

568 Carr, J.R., Vieli, A., and Stokes, C. R.: Climatic, oceanic and topographic controls on marine-
569 terminating outlet glacier behavior in north-west Greenland at seasonal to interannual
570 timescales, *Journal of Geophysical Research*, 118, 1210-1226, 2013.

571 Carrivick, J. L., Smith, W. M., Quincey, D. J., and Carver, S. J.: Developments for budget
572 remote sensing in the geosciences, *Geology Today*, 29, 138-143, 2013.

573 d'Oleire-Oltmanns, S., Marzloff, I., Peter, K. D., and Ries, J. B.: Unmanned Aerial Vehicle
574 (UAV) for monitoring soil erosion in Morocco, *Remote Sensing*, 4, 3390–3416, 2012.

575 Enderlin, E. M., and Howat, I. M.: Submarine melt rate estimates for floating termini of
576 Greenland outlet glaciers (2000-2010), *Journal of Glaciology*, 59, 67-75,
577 doi:10.3189/2013jog12j049, 2013.

578 Hambrey, M. J., and Lawson, W.: Structural styles and deformation fields in glaciers: A
579 review, *Deformation of Glacial Materials*, 176, 59-83, doi:10.1144/Gsl.Sp.2000.176.01.06,
580 2000.

581 Hock, R.: Glacier melt: a review on processes and their modelling. *Progr. Phys. Geogr.*,
582 29(3), 362–391, 2005.

583 Holland, D. M., Thomas, R. H., De Young, B., Ribergaard, M. H., and Lyberth, B.:
584 Acceleration of Jakobshavn Isbrae triggered by warm subsurface ocean waters, *Nature*
585 *Geoscience*, 1, 659-664, doi:10.1038/Ngeo316, 2008.

586 Howat, I. M., Joughin, I., and Scambos, T. A.: Rapid changes in ice discharge from
587 Greenland outlet glaciers, *Science*, 315, 1559-1561, doi: 10.1126/science.1138478, 2007.

588 Howat, I. M., Box, J. E., Ahn, Y., Herrington, A., and McFadden, E. M.: Seasonal variability
589 in the dynamics of marine-terminating outlet glaciers in Greenland, *Journal of Glaciology*,
590 56, 601-613, 2010.

591 Howat, I. M., Negrete, A., Smith, B. E.: The Greenland Ice Mapping Project (GIMP) land
592 classification and surface elevation datasets, *The Cryosphere Discuss*, 8, 1-26,
593 doi:10.5194/tcd-8-1-2014, 2014.

594 Hubbard, A.: The Times Atlas and actual Greenland ice loss, *Geology Today*, 27, 214-217,
595 2011.

596 Hugenholtz, C. H., Levin, N., Barchyn, T. E., and Baddock, M. C.: Remote sensing and
597 spatial analysis of aeolian sand dunes: A review and outlook, *Earth-Science Reviews*, 111,
598 319-334, doi:10.1016/j.earscirev.2011.11.006, 2012.

599 Hugenholtz, C. H., Whitehead, K., Brown, O. W., Barchyn, T. E., Moorman, B. J., LeClair,
600 A., Riddell, K., and Hamilton, T.: Geomorphological mapping with a small unmanned
601 aircraft system (sUAS): Feature detection and accuracy assessment of a photogrammetrically-
602 derived digital terrain model, *Geomorphology*, 194, 16-24,
603 doi:10.1016/j.geomorph.2013.03.023, 2013.

604 Jamieson, S. S. R., Vieli, A., Livingstone, S. J., Cofaigh, C. O., Stokes, C., Hillenbrand, C.
605 D., and Dowdeswell, J. A.: Ice-stream stability on a reverse bed slope, *Nature Geoscience*, 5,
606 799-802, doi:10.1038/Ngeo1600, 2012.

607 Joughin, I., Das, S. B., King, M. A., Smith, B. E., Howat, I. M., and Moon, T.: Seasonal
608 speedup along the western flank of the Greenland ice sheet, *Science*, 320, 781-783,
609 doi:10.1126/science.1153288, 2008.

610 Joughin, I., Smith, B. E., Howat, I. M., Scambos, T., and Moon, T.: Greenland flow
611 variability from ice-sheet-wide velocity mapping, *Journal of Glaciology*, 56, 415-430, 2010.

612 Joughin, I., Smith, B. E., Howat, I. M., Floricioiu, D., Alley, R. B., Truffer, M., and
613 Fahnestock, M.: Seasonal to decadal scale variations in the surface velocity of Jakobshavn
614 Isbrae, Greenland: Observation and model-based analysis, *Journal of Geophysical Research-*
615 *Earth Surface*, 117, doi:10.1029/2011jgf002110, 2012.

616 Jung, J., Box, J. E., Balog, J. D., Ahn, Y., Decker, D. T., Hawbecker, P.: Greenland glacier
617 calving rates from Extreme Ice Survey (EIS) time lapse photogrammetry. C23B-0628,
618 American Geophysical Union, San Francisco, 2010.

619 Kargel, J. S., Ahlström, A. P., Alley, R. B., Bamber, J. L., Benham, T. J., Box, J. E., Chen,
620 C., Christoffersen, P., Citterio, M., Cogley, J. G., Jiskoot, H., Leonard, G. J., Morin, P.,
621 Scambos, T., Sheldon, T., and Willis, I. 2012.: Brief communication. Greenland's shrinking
622 ice cover: "fast times" but not that fast, *The Cryosphere*, 6, 533-537, doi:10.5194/tc-6-533-
623 2012, 2012.

624 Lucieer, A., Turner, D., King, D. H., and Robinson, S. A.: Using an unmanned aerial vehicle
625 (UAV) to capture micro-topography of Antarctic moss beds, *International Journal of Applied*
626 *Earth Observation and Geoinformation*, 27, 53-62, doi:10.1016/j.jag.2013.05.011, 2014.

627 Luckman, A., Murray, T., de Lange, R., and Hanna, E.: Rapid and synchronous ice-dynamic
628 changes in East Greenland, *Geophysical Research Letters*, 33, doi 10.1059/2005gl025048,
629 2006.

630 Moon, T., and Joughin, I.: Changes in ice front position on Greenland's outlet glaciers from
631 1992 to 2007, *Journal of Geophysical Research-Earth Surface*, 113,
632 doi:10.1029/2007jf000927, 2008.

633 Mottram, R. H., and Benn, D. I.: Testing crevasse-depth models: A field study at
634 Breioamerkurjokull, Iceland, *Journal of Glaciology*, 55, 746-752,
635 doi:10.3189/002214309789470905, 2009.

636 Motyka, R. J., Truffer, M., Fahnestock, M., Mortensen, J., Rysgaard, S., and Howat, I.:
637 Submarine melting of the 1985 Jakobshavn Isbrae floating tongue and the triggering of the
638 current retreat, *Journal of Geophysical Research-Earth Surface*, 116,
639 doi:10.1029/2009jf001632, 2011.

640 O'Neel, S., Pfeffer, W. T., Krimmel, R., and Meier, M.: Evolving force balance at columbia
641 glacier, alaska, during its rapid retreat, *Journal of Geophysical Research-Earth Surface*, 110,
642 doi:10.1029/2005jf000292, 2005.

643 Pfeffer, W. T.: A simple mechanism for irreversible tidewater glacier retreat, *Journal of*
644 *Geophysical Research-Earth Surface*, 112, doi:10.1029/2006jf000590, 2007.

645 Raymond, C.: Shear margins in glaciers and ice sheets, *Journal of Glaciology*, 42, 90-102,
646 1996.

647 Rignot, E., Koppes, M., and Velicogna, I.: Rapid submarine melting of the calving faces of
648 West Greenland glaciers, *Nature Geoscience*, 3, 187-191, doi:10.1038/Ngeo765, 2010.

649 Schild, K. M., and Hamilton, G. S.: Seasonal variations of outlet glacier terminus position in
650 Greenland, *Journal of Glaciology*, 59, 759-770, doi:10.3189/2013jog12j238, 2013.

651 Sundal, A. V., Shepherd, A., van den Broeke, M., Van Angelen, J., Gourmelen, N., and Park,
652 J.: Controls on short-term variations in Greenland glacier dynamics, *Journal of Glaciology*,
653 59, 883-892, doi:10.3189/2013jog13j019, 2013.

654 Ullman, S.: The interpretation of structure from motion, *Proceedings of the Royal Society of*
655 *London B203*, 405–426, 1979.

656 Verhoeven, G.: Taking computer vision aloft – archaeological three-dimensional
657 reconstructions from aerial photographs with Photoscan, *Archaeological Prospection*, 18, 67–
658 73, 2011.

659 Vieli, A., Funk, M., and Blatter, H.: Tidewater glaciers: Frontal flow acceleration and basal
660 sliding, *Annals of Glaciology*, 31, 2000, 31, 217-221, doi:10.3189/172756400781820417,
661 2000.

662 Xu, Y., Rignot, E., Fenty, I., Menemenlis, D., and Flexas, M. M.: Subaqueous melting of
663 Store Glacier, West Greenland from three-dimensional, high-resolution numerical modeling
664 and ocean observations, *Geophysical Research Letters*, 40, 4648-4653,
665 doi:10.1002/Grl.50825, 2013.

666 Walter, J. I., Box, J. E., Tulaczyk, S., Brodsky, E. E., Howat, I. M., Ahn, Y., and Brown, A.:
667 Oceanic mechanical forcing of a marine-terminating Greenland glacier, *Annals of*
668 *Glaciology*, 53, 181-192, doi:10.3189/2012aog60a083, 2012.

669 Weertman, J.: Can a water-filled crevasse reach the bottom surface of a glacier?, *IAHS Publ.*,
670 95, 139–145, 1973.

671 Whitehead, K., Moorman, B. J., and Hugenholtz, C. H.: Brief communication: Low-cost, on-
672 demand aerial photogrammetry for glaciological measurement, *Cryosphere*, 7, 1879-1884,
673 doi:10.5194/tc-7-1879-2013, 2013.

674 Weidick, A.: Greenland, with a section on Landsat images of Greenland, in, *Satellite image*
675 *atlas of glaciers of the world*, Williams, R. S., and Ferrigno, J.G. eds, US Geological Survey,
676 Washington, DC, C1–C105 (USGS Professional Paper 1386-C), 1995.

677